Journal of Medical Imaging

MedicalImaging.SPIEDigitalLibrary.org

Toward quantitative quasistatic elastography with a gravity-induced deformation source for image-guided breast surgery

Rebekah H. Griesenauer
Jared A. Weis
Lori R. Arlinghaus
Ingrid M. Meszoely
Michael I. Miga

SPIE.

Rebekah H. Griesenauer, Jared A. Weis, Lori R. Arlinghaus, Ingrid M. Meszoely, Michael I. Miga, "Toward quantitative quasistatic elastography with a gravity-induced deformation source for image-guided breast surgery," *J. Med. Imag.* **5**(1), 015003 (2018), doi: 10.1117/1.JMI.5.1.015003.

Journal of Medical Imaging 5(1), 015003 (Jan–Mar 2018)

Toward quantitative quasistatic elastography with a gravity-induced deformation source for image-guided breast surgery

Rebekah H. Griesenauer,[a] Jared A. Weis,[b] Lori R. Arlinghaus,[c] Ingrid M. Meszoely,[d] and Michael I. Miga[a,c,e,f,g,*]
[a]Vanderbilt University, Department of Biomedical Engineering, Nashville, Tennessee, United States
[b]Wake Forest School of Medicine, Department of Biomedical Engineering, Winston Salem, North Carolina, United States
[c]Vanderbilt University Medical Center, Vanderbilt University Institute of Imaging Science, Nashville, Tennessee, United States
[d]Vanderbilt University Medical Center, Department of Surgery, Nashville, Tennessee, United States
[e]Vanderbilt University, Vanderbilt Institute for Surgery and Engineering, Nashville, Tennessee, United States
[f]Vanderbilt University Medical Center, Department of Radiology and Radiological Sciences, Nashville, Tennessee, United States
[g]Vanderbilt University Medical Center, Department of Neurological Surgery, Nashville, Tennessee, United States

Abstract. Biomechanical breast models have been employed for applications in image registration and diagnostic analysis, breast augmentation simulation, and for surgical and biopsy guidance. Accurate applications of stress–strain relationships of tissue within the breast can improve the accuracy of biomechanical models that attempt to simulate breast deformations. Reported stiffness values for adipose, glandular, and cancerous tissue types vary greatly. Variations in reported stiffness properties have been attributed to differences in testing methodologies and assumptions, measurement errors, and natural interpatient differences in tissue elasticity. Therefore, the ability to determine patient-specific *in vivo* breast tissue properties would be advantageous for these procedural applications. While some *in vivo* elastography methods are not quantitative and others do not measure material properties under deformation conditions that are appropriate to the application of concern, in this study, we developed an elasticity estimation method that is performed using deformations representative of supine therapeutic procedures. More specifically, reconstruction of mechanical properties appropriate for the standard-of-care supine lumpectomy was performed by iteratively fitting two anatomical images before and after deformations taking place in the supine breast configuration. The method proposed is workflow-friendly, quantitative, and uses a noncontact, gravity-induced deformation source. [DOI: 10.1117/1.JMI.5.1.015003]

Keywords: elastography; magnetic resonance imaging; lumpectomy; image guidance; biomechanical modeling; registration; breast cancer.

Paper 17319PR received Oct. 27, 2017; accepted for publication Jan. 15, 2018; published online Feb. 8, 2018.

1 Introduction

Breast cancer imaging modalities include x-ray mammography, ultrasound, and magnetic resonance imaging (MRI). In each modality, unique patient positioning or the nature of mechanical excitation confounds the use of these diagnostic images for surgical guidance. For example, in x-ray mammography, the patient stands erect with the breasts compressed between two plates. During ultrasound exams, the patient is positioned supine with the ipsilateral arm placed above the patient's head. MRI exams of the breast are typically performed with the patient lying prone with breasts pendant in the MRI coil chambers. During surgery, the patient is positioned supine with the ipsilateral arm placed perpendicular to the body. Each modality has unique benefits for the screening, diagnosis, and staging of breast cancer. However, there is certainly varied utility in the use of these data for localizing tumors during surgery. For breast-conserving therapy (BCT), which consists of a lumpectomy (removal of tumor and small amount of surrounding healthy tissue) followed by radiation therapy, localization of the tumor during surgery can be difficult. Reoperations due to the presence of residual tumor after an initial resection average 16.5% to 40%.[1–5] Furthermore, ductal carcinoma *in situ* (DCIS) is associated with a threefold increase in reoperation rates when compared to invasive carcinomas.[6] DCIS lesions have diffuse growth patterns and ill-defined margins when compared to invasive breast cancers.[7] Furthermore, DCIS extensions into intraductal tissue can be difficult to determine. Due to the mainstream usage of screening mammography, an increasing number of patients are being diagnosed with DCIS and early stage cancers. Therefore, precise strategies to localize the nonpalpable DCIS lesions are needed. While intraoperative ultrasound has been shown to reduce the need for re-excisions,[8] ultrasound cannot image most cases of DCIS and is limited in detecting multifocal disease, bilateral breast cancers, and intraductal spread characteristics.[9]

While MRI is considered the most sensitive and accurate imaging modality in the context of breast cancer,[10,11] the limited specificity of MRI provides some areas of improvement. There is some evidence that preoperative MRI causes over treatment and is associated with an increase in the use of mastectomy, delay in treatment, and an increase in the number of additional biopsies.[12–14] Alternatively, several studies have

*Address all correspondence to: Michael I. Miga, E-mail: michael.i.miga@vanderbilt.edu

2329-4302/2018/$25.00 © 2018 SPIE

disputed these claims arguing that MRI provides invaluable information regarding the extent of disease. In a recent prospective, randomized, and multicenter study, a significant decrease in reoperation rates was reported between women who received a preoperative staging MRI and women who did not receive an MRI prior to lumpectomy.[15] Sung et al.[16] published a retrospective analysis that concluded that reoperation rates among BCT patients were lower for women who received a preoperative MRI. Several other studies report positive findings for improved preoperative staging using MRI.[15–18] Overall, the argument surrounding the value of preoperative MRI remains somewhat unclear. However, it is generally agreed upon that MRI provides the most accurate delineation of the size and extent of cancer and offers the highest sensitivity for intraductal extension involved in breast cancers.[19–21]

Regardless, these diagnostic MR images are not particularly useful in the context of surgical planning and guidance currently. As previously discussed, preoperative MR images are acquired in the prone position with pendant breasts while surgery is performed with the patient lying supine. Several studies have reported significant displacements in breast tumors between the prone and supine positions in the order of 18 to 60 mm.[22,23] A more direct approach is to use MR images taken in the supine position to guide surgery. Supine breast imaging has been a topic of interest in several studies,[24–26] including the use of intraoperative MRI.[27] In the work by Mallory et al.,[27] intraoperative supine MRI for breast surgery planning was shown to be feasible while also demonstrating limitations for the use of prone MRI in surgical planning. However, intraoperative MRI surgical suites are rare in the United States, thus making this approach difficult to translate across healthcare institutions. The use of supine breast MRI in the context of image-guided breast surgery (IGBS) has been suggested in several frameworks.[22,28–30] Image-guided surgery, or frameless stereotaxy, relates the location of surgical instruments in the operating room to preoperative imaging data. These systems are the clinical gold standard for performing neurosurgery and have been adapted for use in the liver,[31] kidney,[32] and lungs.[33] Biomechanical models are used in many of these systems to correct for organ deformation during surgery.[34] Commercial systems, such as SonoWand™ and BK Ultrasound systems, are also emerging for real-time image fusion of intraoperative ultrasound and preoperative imaging data to account for organ deformation during surgery.

In the context of IGBS, preoperative supine breast images are registered to the physical space of the operating room to act as patient-specific maps to assist surgeons in localizing discrete breast lesions. The patient-specific aspect of these systems involves the creation of biomechanical computational models to correct for deformation that naturally occurs between the preoperative image and surgical space breast geometries. In this study, we developed a method to further optimize the patient-specific parameters of IGBS systems. In Fig. 1, the basic steps for IGBS are shown. The process begins with preoperative imaging of the breast in the supine position. Anatomical and morphological images are obtained at this step. Preprocessing of these images include segmentation of the breast tissue into adipose, fibroglandular, chest wall muscle, and tumor. From here, a finite-element method (FEM) model is created to simulate breast tissue deformation during the intraoperative registration step. In the intraoperative registration step, the surface of the breast is digitized by an optical tracking system, and a biomechanically assisted nonrigid registration is performed to render the preoperative data into the physical space of the operating room. Once this registration is complete, a guidance display of the coregistered preoperative image data is used to localize tumors and map out surgical plans. The extra step we have added and that will be elaborated upon in this study is during the preprocessing step. Here, we estimate the material properties of the patient's breast tissue to be incorporated into the biomechanical model for improved accuracy.

An IGBS compatible stiffness estimation method was recently introduced[35] that relies on gravity-induced deformations of the breast captured in an additional 2-min MRI scan. In that work, parameter sweeps were performed, sampling stiffness values for adipose and fibroglandular tissue. A biomechanical model was solved for each adipose–fibroglandular stiffness value set. The displacement field generated by the model was then used to deform the gravity-induced excitation image. A measure of image similarity was then calculated between the model-deformed image and the baseline image for each adipose–fibroglandular stiffness value set. While the framework for the stiffness estimation method was tested and shown to be promising for work in IGBS, performing a parameter sweep on a sufficient search space with acceptable discretization of said search space is extremely time consuming. Therefore, in this study, we perform an investigation into the use of optimization routines to reconstruct the values of patient-specific

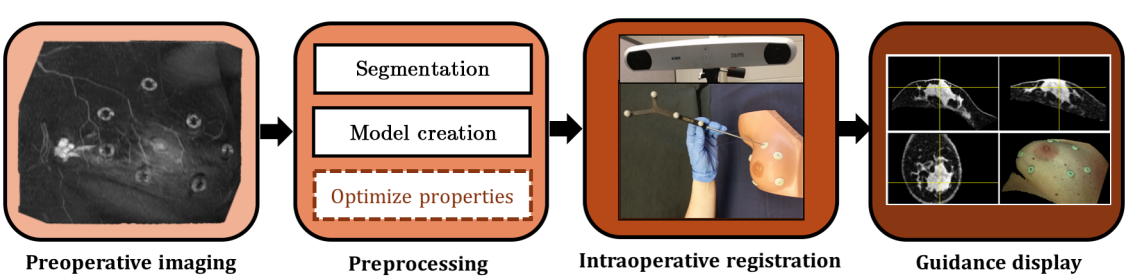

Fig. 1 General framework for IGBS. The process begins with preoperative imaging of the patient breast in the supine position. The preoperative imaging panel shows a representative MR volume rendering of a contrast-enhanced supine breast of a patient with breast cancer. The rendering shows a tumor with elevated image intensity and ring-shaped adhesive surface fiducials used during the intraoperative registration step. Preprocessing is performed after imaging, prior to surgery. At this step, patient-specific stiffness properties are extracted to optimize the patient-specific model. Intraoperative registration is performed to transform the preoperative image and patient-specific model into surgical space. Finally, the guidance display is used by the surgical team to localize tumors.

breast tissue stiffness. An interesting set of observations was reported in Ref. 35 that prompted this investigation. For example, the shape of the objective function changes according to the fibroglandular content of the breast and the magnitude of deformation induced during gravity excitation. Due to inevitable differences in patient breast size, fibroglandular content, deformation levels, and stiffness values, we opted to test optimization methods to determine the most appropriate method to use going forward in the context of IGBS. In this study, simulation data were generated and human data were collected to test optimization performance. Furthermore, an exploration of this stiffness estimation method for reconstructing a heterogeneous distribution of properties within the breast was performed.

2 Methods

2.1 *Overview of Stiffness Estimation Method*

Optimization of patient-specific breast tissue stiffness begins with the acquisition of two gravity-loaded supine breast MR images. The baseline image is acquired with the patient lying supine with the ipsilateral arm placed above her head. Gravity excitation is produced by placing a foam wedge posterior to the breast being imaged. This causes a rotation about the longitudinal axis of the body which results in tissue deformation due to changes in tissue weight distributions with respect to gravity. From the gravity-excited image, an FEM model is created. In this framework, the chest wall is assumed to be a reliably rigid structure and is used to align the baseline and gravity-excited images. The chest wall in each image is segmented, and a rigid registration is performed by maximizing the image similarity between the chest walls in each space. The transformation matrix yielded by this chest wall registration is used to transform the baseline image into the gravity-excited space. Now, the chest walls in each space are aligned and the resulting misalignment of the breast tissue is due to the nonrigid deformation caused by differences in gravitational loading. Also from the chest wall alignment, the differences in gravitational loading are quantified by using the rotational component of the transformation matrix to calculate the relative change in the acting gravity direction. The rotated gravity vector is applied as a body force of tissue weight in the biomechanical model. A biomechanical model is then solved to obtain a displacement field. The displacement field is interpolated onto the gravity-excited image to create a model-deformed image. Material properties are iteratively updated within an optimization routine until the model-deformed image matches the chest wall-aligned baseline image. A visual representation of this process is shown in Fig. 2 and more descriptive detail of the general framework can be found in Ref. 35.

An FEM tetrahedral mesh was created from the gravity-excited image (nominal edge length = 3 mm). The difference in gravitational loading was approximated by calculating a gravity vector: $\mathbf{g}_{\text{rotated}} = \mathbf{g}_{\text{baseline}} - R \times \mathbf{g}_{\text{baseline}}$, where $\mathbf{g}_{\text{baseline}}$ was assumed to be unit vector normal to the MR table and R is the rotation matrix generated from the rigid chest wall alignment. A body force of tissue weight $(9.8\ \text{m/s}^2 \times \mathbf{g}_{\text{rotated}} \times \rho)$ was applied in a biomechanical model that assumes isotropic and Hookean linear elastic behavior. Tissue density, ρ, was estimated at 1000 kg/m^3. Nodal positions corresponding to the chest wall were prescribed a fixed Dirichlet boundary condition with the assumption that the chest wall remains relatively static between the two configurations. Using these parameters, a forward biomechanical model with a nonlinear, corotational finite-element framework[36] was solved to obtain a displacement field. The displacement field was used to deform the gravity-excited image. An optimization procedure iteratively updates the stiffness properties of the breast tissue until the model-deformed image matches the baseline image. An expanded description of the methods involved in this approach can be found in Ref. 35.

2.2 *Human Volunteer Data*

With IRB approval and informed consent, five healthy volunteers were enrolled to participate in this imaging study. The left and right breasts of three volunteers were scanned in a separate imaging setup to comprise a total of eight datasets. Furthermore, the left breast of the first volunteer was scanned

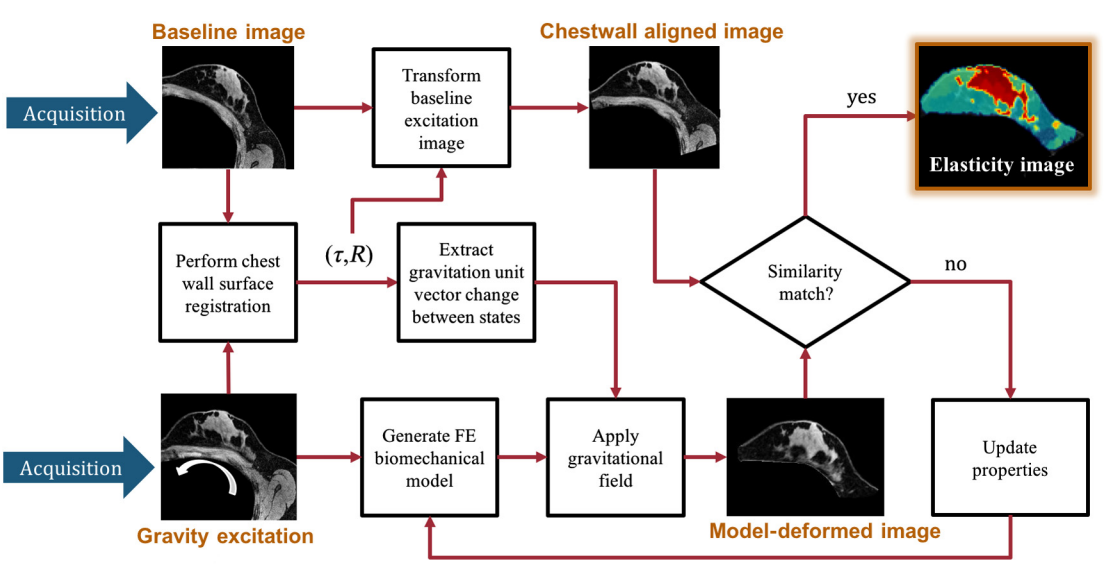

Fig. 2 Overview of the process to optimize patient-specific material properties. The algorithm estimates tissue elasticity by fitting two acquired anatomical images by minimizing a similarity metric between an experimentally acquired image and a model-deformed image.

twice in a test–retest setup to evaluate reproducibility of heterogeneous property reconstruction. While anecdotally suggested, the quantitative stiffness of each breast was assumed to be unique. A baseline and gravity-excited image was acquired in a Philips 3T Achieva MR scanner using a SENSE XL Torso Coil (Philips Healthcare, Best, The Netherlands) with the following parameters: T_1-weighted, 3-D turbo field echo sequence with fat suppression, a field of view of 200 mm × 200 mm × 160 mm, reconstructed voxel size of 0.391 mm × 0.391 mm × 1 mm, TR/TE = 7.40/3.91 ms, and flip angle = 20 deg using SENSE parallel imaging (acceleration factor = 2).

2.3 *Simulation Data*

A simulation study was performed to assess the performance of the optimization methods with minimal noise contributions and to determine a representative true form of the objective function using similar clinical parameters. Model parameters were selected to form a representative simulated clinical dataset. These parameters include: 500 and 2000 Pa for the stiffness of adipose and glandular tissue, respectively, a Poisson's ratio of 0.45, tissue density of 1000 kg/m^3, and a rotation relative to the initial direction of gravity ($\mathbf{g}_{\text{rotated}}$) of 15 deg. Using baseline images from five healthy volunteers with a range of fibroglandular content (8%, 12%, 20%, 30%, and 40%), a forward model was solved with these simulation parameters and the resulting displacement field was interpolated onto the baseline image to create a simulated gravity-excited image. Figure 3 shows representative baseline and simulation images and the corresponding deformation that drives the stiffness estimation procedure.

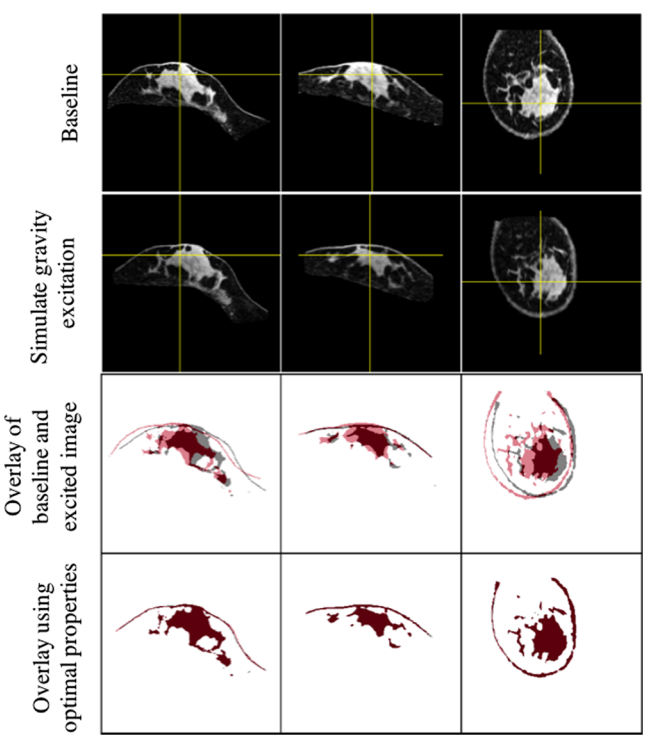

Fig. 3 Representative images used in simulation study. The top row contains axial, sagittal, and coronal views of a baseline image. The middle row shows the same three orthogonal slices of the simulated gravity-induced configuration image. The third row displays the simulated gravity-induced image as a red mask and baseline image as a gray mask. The fourth row displays the simulated gravity-induced configuration and model-deformed image using optimized reconstructed properties. The overlay of the baseline and gravity-excited image masks demonstrates the type of deformation yielded from the gravity-induced excitation used in this method.

2.4 *Optimization Procedures*

Two optimization methods were studied along with a fine parameter sweep to identify the best methods to obtain patient-specific stiffness properties of breast tissue. There are several well-established optimization procedures to minimize the mismatch between the baseline image and model-deformed image and update material parameters. In previous explorations of similar work, we found a conjugate gradient (CG) method[37] and the Levenberg–Marquardt (LM) algorithm[38] to be promising. Therefore, we tested both the CG method and LM method in this study. A very brief overview of each method is given below.

The steepest descent method reduces the sum of the squared errors by updating the optimization parameters in the direction of the greatest reduction of the least squares objective

$$\psi = |S_{\text{TRUE}} - S_{\text{EST}}|^2, \tag{1}$$

where S_{TRUE} and S_{EST} are the similarity correlation coefficient values for the ideal similarity (i.e., experimentally deformed acquired image volume and itself) and the similarity between experimentally deformed and model-deformed image volumes, respectively. With respect to the steepest descent method, it is a line search method that takes an initial guess and calculates the function gradient producing a search direction of the steepest descent. Gradient descent methods are slow to converge especially when close to the minimum. The CG method[39,40] improves the method of steepest descent by reducing repetitious iteration steps. The CG method takes orthogonal steps to the function minimum which reduces step redundancies. Due to the reduction in iterations needed, CG methods are valuable for large dimension optimization problems. In this study, the gradient was calculated using a central-difference approximation and was performed using a custom implementation of the algorithm.

Alternatively, in LM,[41,42] the method takes advantage of the gradient descent at early iterations to improve its radius of convergence and then accelerates to a Gauss–Newton optimization (a quadratically convergent fixed point method) method when estimated values are near their optimum. The Gauss–Newton algorithm may not converge if the initial guess is far from the optimal. In this study, the Jacobian associated with the LM method was calculated using a forward-difference gradient calculation (requiring one model solve per optimization variable). The LM method was implemented using MATLAB® R2015 (The MathWorks Inc., Natick, Massachusetts) lsqnonlin function.

To observe material property optimization performance, a parameter sweep was first performed on a moderate search space to obtain an objective function map. The objective function was determined using an image similarity metric calculated in five discrete zones within the image volume. The similarity metric used in Eq. (1) for this study was Pearson's correlation coefficient. The root mean squared (RMS) nodal displacement error was also calculated during the simulation parameter sweep to provide some added understanding of how material property

Table 1 Reconstruction results for simulation data. Mean (standard deviation) values are reported in Pa for each simulation case.

	LM		CG	
	Adipose	Glandular	Adipose	Glandular
8% Glandular tissue	500.2(0.81)	1992.0 (35.5)	501.2 (5.5)	1998.2 (127.8)
12% Glandular tissue	499.9(0.53)	2002.7 (11.1)	499.2 (1.7)	2006.0 (27.7)
20% Glandular tissue	500.6(1.48)	1989.3 (24.4)	501.25 (1.5)	1976 (29.1)
30% Glandular tissue	500.1(0.33)	1999.9 (0.81)	500 (0)	1999.3 (0.26)
40% Glandular tissue	499.5(0.58)	2000.8 (2.17)	499.5 (0.99)	1999.35 (3.42)

reconstruction variability affects registration fidelity. Clearly, the RMS nodal displacement errors could not be studied during the *in vivo* human subject parameter sweep because known correspondence of tissue features is unavailable. In the simulation study, the search space for the parameters sweeps was 100 to 1000 Pa for adipose and 400 to 4000 Pa for glandular tissue. The step size for each tissue type was 50 Pa for adipose tissue and 50 Pa for glandular tissue. In the human volunteer study, the parameter search space was 100 to 1000 Pa for adipose tissue and 100 to 10,000 Pa for glandular tissue with step sizes of 25 Pa for adipose and 50 Pa for glandular.

After the parameter sweep was performed, an estimation of the true minimum was obtained by taking the minimum value of the objective function map. Due to large variations in breast stiffness, volume, and fibroglandular content, a range of initial guesses were used for the optimization procedures to maximize successful convergence despite differences in the shape of the objective function maps and assess the fidelity of the optimization procedure. The initial guesses were distributed around the ground truth values for the simulation data. For the human datasets, the following starting points were used as initial guesses: (1) 2000 Pa for adipose and 2000 Pa for glandular, (2) 500 Pa for adipose and 500 Pa for glandular, (3) 500 Pa for adipose and 2000 Pa for glandular, and (4) 100 Pa for adipose and 4000 Pa for glandular.

3 Results

3.1 *Simulation Data*

The average solve time for the simulation data was 112.6 ± 63.8 s. The solve time was defined as the total time it takes to perform one forward model solve with a given property set (with three corotational iterations), deform the image, and calculate the objective function. From this, the average time to perform a parameter sweep is estimated. For the simulation parameter sweep performed in this study, a total of 1482 solves were executed. This translates to 46.3 h if solved in series. If the search space were to be expanded (such as in the human case) or if the step size were to be decreased for a more resolved error map, the number of model solves required to create the map would increase significantly. This fact illustrates the importance of performing an optimization procedure to obtain the objective function minimum. Property optimization for the simulation data was in general quite robust, with all but one of the initial guess values converging to the minimum for the simulation data for both the LM and CG methods. Table 1 shows the average and standard deviations of the converged reconstructed values in simulation for each case. Figure 4 shows the tissue stiffness reconstruction results for the simulation data using the LM method. The grayscale contour map shows the objective function error map created during the parameter sweep. The colored lines overlaid on the contour plot represent optimization iterations for each initial guess. In Fig. 4(e), the initial guess starting at 500 Pa for glandular and 500 Pa for adipose did not converge to the minimum using the LM method but did converge using the CG method. Figure 5 shows the RMS nodal displacement error maps for the 12% and 20% fibroglandular simulation datasets. These error maps represent the true form of the objective function as they were calculated with absolute knowledge of point correspondences. The 12% and 20% glandular simulation datasets were the most representative of clinical data, as the percent fibroglandular content of our clinical datasets was 18.3 ± 8.7 (min = 7.7% and max = 32%). Furthermore, a study looking at the breast density of 230 women ages 32 to 77 reported a range of 7% to 28% fibroglandular tissue content.[43]

3.2 *Human Data*

The average solve time (includes a forward model solve with three corotational iterations, image deformation, and correlation calculation) for the human datasets was 107.8 ± 26 s. From this, the average time to perform a parameter sweep was estimated. The total number of solves for the human dataset parameter sweep was 7722. Therefore, if the object function error map was to be created in series, the total solve time for the parameter sweep would be 231.2 h. This again illustrates the importance of an optimization procedure to find the optimal set of stiffness values.

Figure 6 shows three representative results for the human data reconstruction. Figures 6(a) and 6(d) correspond to case 1, Figs. 6(b) and 6(e) represent case 4, and Figs. 6(c) and 6(f) correspond to case 5. Here, two representative optimization initial guesses are shown for each case [initial guess at (500, 500) and (2000, 2000)].

The objective function value per iteration is shown in Figs. 6(d)–6(f), while the downward path taken by the optimization procedure is shown overlaid on the parameter sweep error maps in Figs. 6(a)–6(c). For the human datasets, the minimum objective function value was selected out of all initial guess optimization runs. The minimum objective function and corresponding stiffness values were used to populate Table 2. The parameter sweeps and optimization results for eight unique

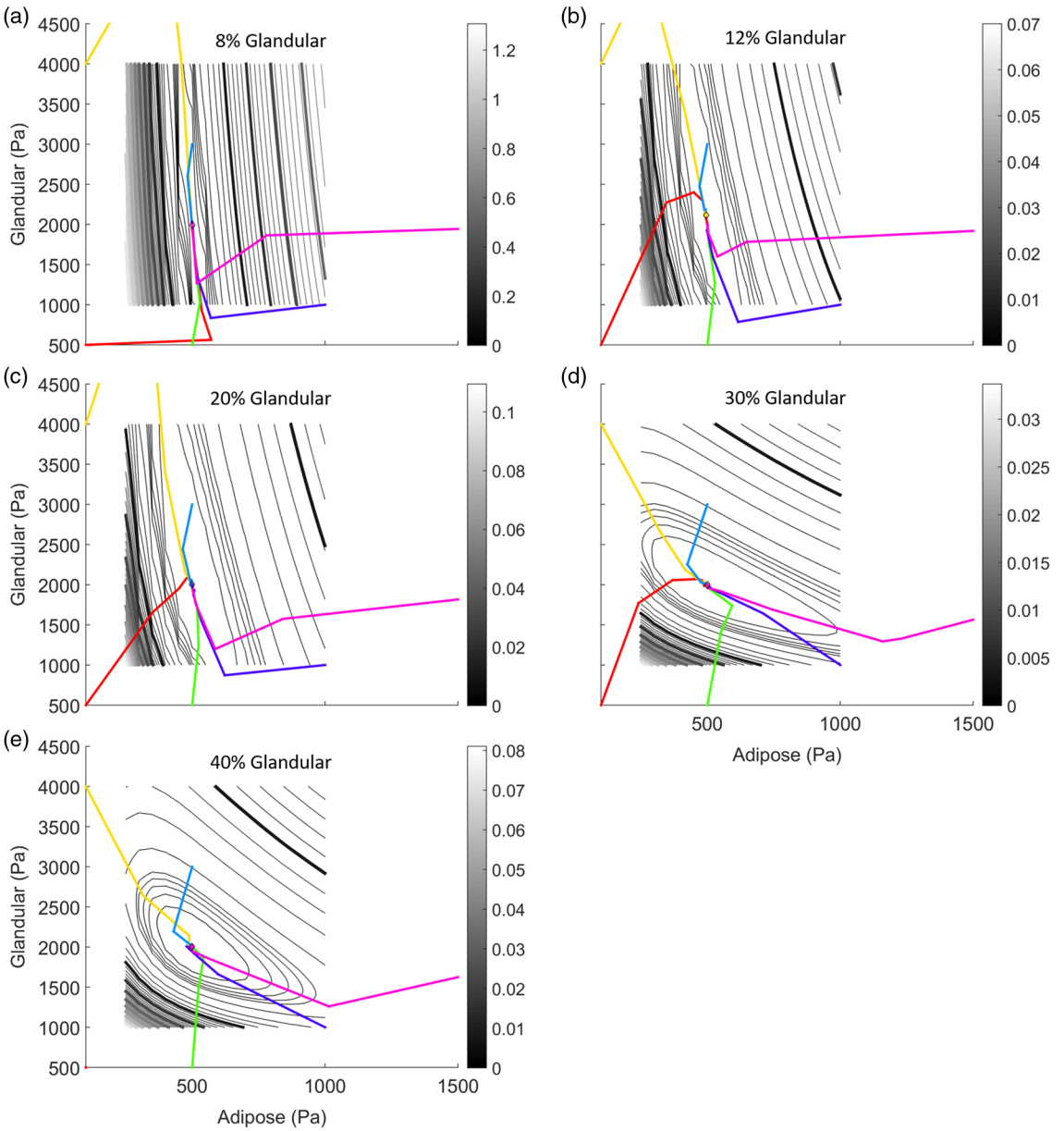

Fig. 4 Tissue stiffness reconstruction results for simulation data. Each plot represents a simulation dataset with a range of fibroglandular content (a) 8%, (b) 12%, (c) 20%, (d) 30%, and (e) 40%. The grayscale contour map is the objective function error map created from the parameter sweep. The contour values represent the objective function value at each adipose–glandular combination solved. The colored lines show the optimization iterations and results for the LM method. Convergence sensitivity of the optimization was tested using a range of initial guesses (depicted as different colored lines overlaid on the error maps).

breast datasets are shown in Table 2. For each case, the global optimal properties were selected based on the overall minimum objective function value. These optimal properties are highlighted in bold in Table 2. The CG method outperformed the LM method in most cases, with the parameter sweep maintaining the minimum for three cases. For all cases, the CG optimization achieved less than a 20% difference when compared to the parameter sweep minimums. In six cases, the CG optimization procedure found a lower minimum than the parameter sweep. In the three cases in which the CG method did not find a lower minimum, the percent errors from the parameter sweep values ranged from 0.8% to 11.5% for adipose tissue and 13% to 18.3% for fibroglandular tissue.

3.3 *Elastographic Approach to Stiffness Estimation*

A step toward heterogeneous determination of breast tissue mechanical properties was performed. Rather than classifying tissues as either adipose or glandular, in this experiment, the breast was discretized into 20 unique regions (10 glandular regions and 10 adipose regions). Each region was introduced as a degree of freedom in the optimization routine. The optimization minimized an objective function consisting of 10 zone-based correlation coefficients within the image volume that represents the residual error between the model-deformed image and the acquired baseline image. A CG algorithm was used here due to the superior performance of the method in

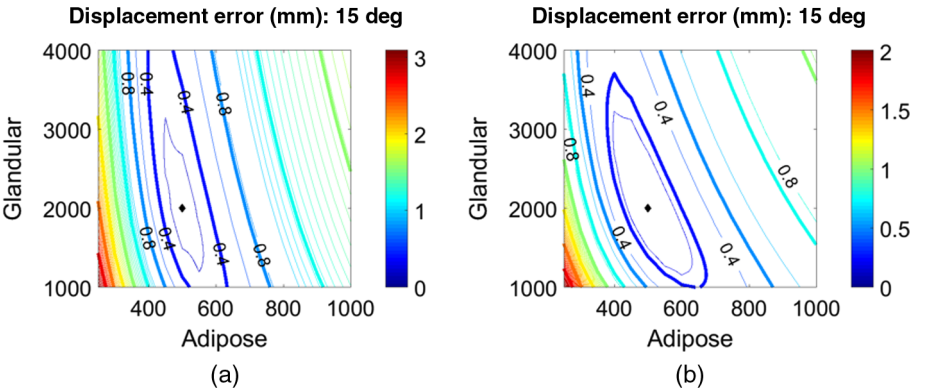

Fig. 5 RMS nodal displacement errors for simulation parameter sweeps for (a) 12% fibroglandular and (b) 20% fibroglandular tissue. The *x*-axis contains the range of stiffness values sampled for adipose tissue. The *y*-axis is the range of stiffness values sampled for glandular tissue. The contour levels represent the nodal displacement error at that adipose–glandular combination. The contour map also shows the 0.4- and 0.8-mm contour levels which roughly corresponds to the half and full voxel sizes of the image volumes used in this study, respectively. The diamond shows the location of the minimum displacement error (i.e., the true property values).

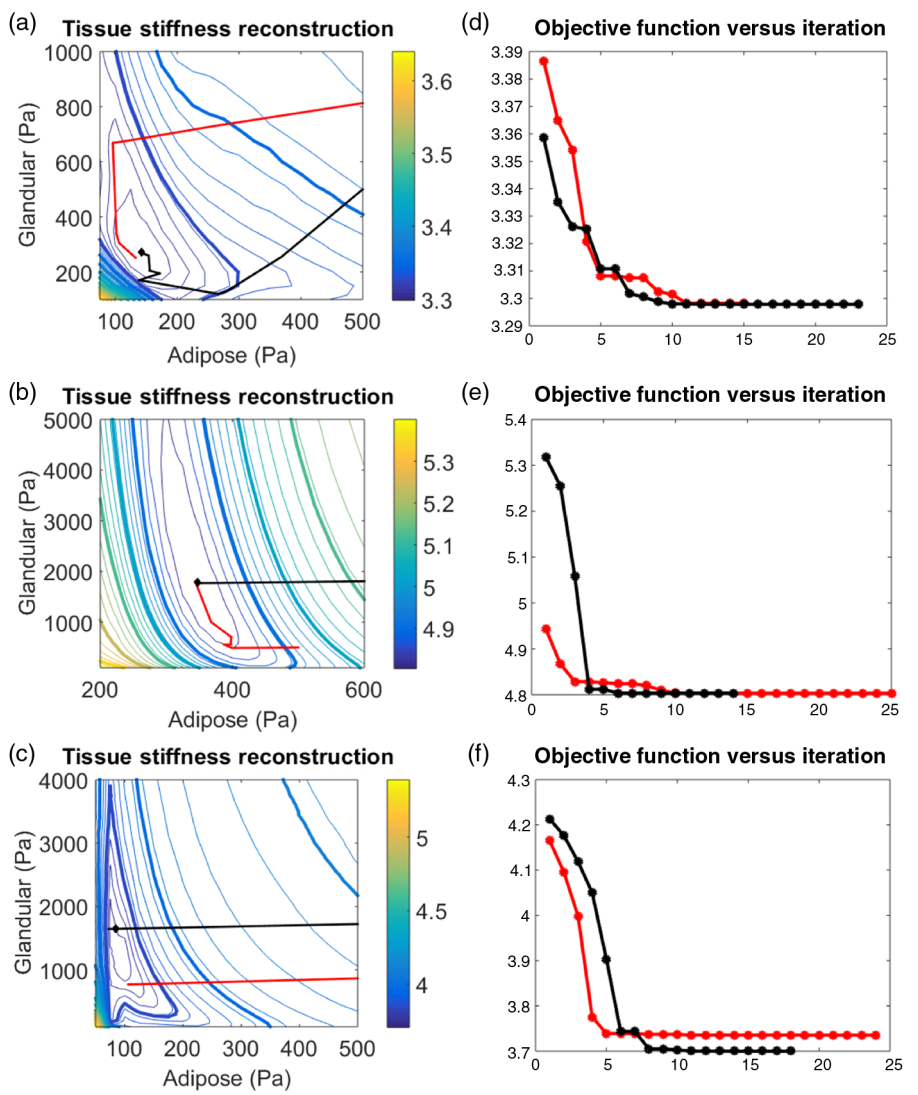

Fig. 6 Summary of human data stiffness property reconstruction results for three different datasets. (a, b, c) contain objective function contour plots demonstrating the shape of the objective function for three datasets. Overlaid onto these contour plots are optimization results for two starting points using the CG algorithm. The starting points shown here are (2000, 2000) and (500, 500). In (d, e, f), the value of the objective function at each iteration is shown for each starting initial guess.

Table 2 Reconstruction results for human data. Table containing parameter sweep and optimization results for the human datasets. All adipose and glandular values are reported in Pa. Note that cases 1 and 2 are of the same breast, acquired in a test–retest setup. The bold values represent the set of fibroglandular–adipose values that resulted in the overall minimal objective function. The solve time was defined as the total time it takes to perform one forward model solve (with three corotational iterations), deform the image, and calculate the objective function.

	Parameter sweep		LM		CG_CD	
Solve time (s)	Adipose	Glandular	Adipose	Glandular	Adipose	Glandular
127.9	350	1650	356.5	1477.5	**347.1**	**1780**
104.4	475	1600	448.3	1971.7	**465**	**1824.9**
94.2	**650**	**6800**	705.1	4165.2	687	5885
105.9	125	250	116.4	285.97	**143.2**	**266.5**
120.3	75	1300	73.1	1451.8	**74.2**	**1576.8**
155.1	**200**	**2350**	198.7	2016.4	201.7	1983.1
167.2	275	4950	274.9	6581.8	**273.9**	**4000.2**
101.7	**675**	**5550**	1248	6293	753.7	6533.6
59.9	100	450	108.2	372.8	**96.2**	**412.7**

human datasets. Similar to Ref. 37, spatial prior constraints were utilized that rely on image intensity knowledge to designate similar tissue types. This anatomical knowledge is used as a soft constraint in the optimization routine, which penalizes large variations among similar tissue types and acts to constrain stiffness values designated as the same tissue type to remain somewhat similar. Following reconstruction, the output is a volumetric distribution of absolute stiffness in each of the

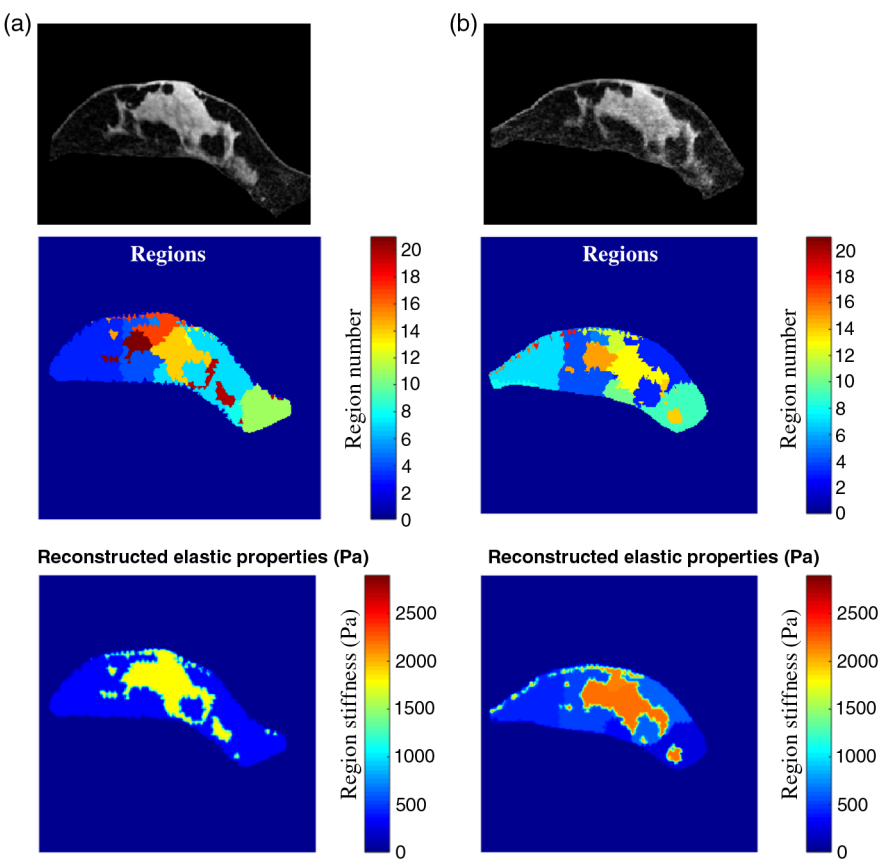

Fig. 7 Test–retest elastography results for (a) case 1 and (b) case 2. The top figures show central axial slices of the gravity-excited anatomical MR image. The middle panels show the breast discretized into 20 unique regions. The bottom row shows the reconstructed property results for each set. The ratio of fibroglandular tissue to adipose tissue was 5.2 for the test set and 4.9 for the retest set.

20 regions. Cases 1 and 2 were used as a test–retest dataset, as they are both the left breast of the same subject. The test–retest dataset was acquired by reproducing the baseline and gravity-excited image in two separate imaging exams. Therefore, these data are unique with respect to each other but represent two examinations of the same breast.

Figure 7 shows the test–retest elastography results. The top panel contains central axial MR slices of the gravity-excited image for the test (a) and retest (b) cases. The middle panel shows the discretization of the breast as 20 regions (10 regions per tissue type). The bottom panel in Fig. 7 shows the reconstructed elastic property values for each region overlaid on a mask of the gravity-excited images. The average reconstructed values for fibroglandular tissue were 1783 Pa for the first test (case 1) and 2196 Pa for the second retest set (case 2). The average test/retest values for adipose tissue were 336/450 Pa. The ratio of average fibroglandular tissue to average adipose tissue for the test/retest sets were 5.2/4.9. The total solve time to reconstruct 20 unique stiffness properties was 13.7 h for the test set and 15.8 h for the retest set.

4 Discussion

In these studies, we investigated the use of optimization routines to facilitate the reconstruction of patient-specific breast tissue stiffness values. In simulation, reconstructed stiffness properties robustly converged to the global minimum despite varying initial guesses. In clinical data, noise is introduced into the system, resulting in convergence of material properties into local minimums. However, with the introduction of four different starting points (initial guesses), an acceptable optimization (<20% error) was obtained in all cases. Figures 6(c) and 6(f) show how one initial guess might find a global minimum while another gets caught in a local minimum. Given the nature of image-guided surgery applications, we estimate that an error of <20% is acceptable. As shown in Fig. 5, these errors are within an acceptable range as they introduce less than a 1 mm error into the overall IGBS system. This can be seen from Fig. 5 where displacement errors between 1600 to 2400 Pa for glandular ($\pm$20% of true glandular value) and 400 and 600 Pa for adipose ($\pm$20% of true adipose value) lie approximately within the 0.8-mm contour level.

Overall, reconstructing patient-specific stiffness parameters was successful using our implementation of the CG algorithm. The number of iterations required to obtain a minimum in the human datasets using the CG method was 14.7 ± 5.6 (min $= 8$ and max $= 23$). Therefore, the CG method can be used to obtain patient-specific breast tissue properties with drastically less model solves than in a parameter sweep (recall the number of model solves in the parameter sweep was 7722). Despite the fact that for each iteration, the CG method requires two model solves per optimization variable to evaluate the gradient, the total number of model solves needed to obtain an optimum is 2 to 3 orders of magnitude less than what is required during the parameter sweep.

The error maps associated with human subject data (Fig. 6) are noisier than their simulation data counterparts (Fig. 4). Furthermore, human data are subject to errors associated with arm-placement-induced breast deformations that are not captured by the purely gravity-based reconstruction model. While care was taken to reproduce the same arm positioning in the baseline and gravity-induced images, further analysis will be performed to investigate the influences of arm position differences. In addition, noise and artifact reduction techniques during the MR image-acquisition phase will be explored. Registration errors induced by motion artifacts are possible. Therefore, techniques to mitigate respiratory noise will be investigated, such as respiratory-triggered supine MR imaging, which can improve the image quality of supine breast images.[44]

Heterogeneous property reconstruction is not feasible using parameter sweep methods as the number of model solves required would be too burdensome. However, with the optimization routine demonstrated in this study, heterogeneous property reconstruction becomes feasible. Here, a step toward heterogeneous property reconstruction was performed using a test–retest dataset. Reconstruction of 20 unique stiffness properties demonstrates the capabilities of expanding this method to include tissue types beyond adipose and fibroglandular, i.e., breast tumors. Selection of optimal discretization (i.e., number of unique regions per tissue type) and methods to reduce solve time will be evaluated in the future when tumor tissue is added. The ratio of fibroglandular tissue to adipose tissue was 5.2 for the test set and 4.9 for the retest set. As shown in Fig. 7, in reconstructing 10 regions for adipose and 10 regions for glandular tissue, little heterogeneity within tissue types was found. While moving to this elastography approach was shown to be feasible, a finer amount of discretization (i.e., more regions) is currently under investigation to resolve stiffness differences within tissue types. Beyond the levels of discretization, the number of zones used during the image similarity calculation and level of spatial prior weighting should be studied to obtain optimal reconstruction behavior.

Other *in vivo* methods to determine patient-specific breast tissue stiffness have been described. These methods include MR elastography,[45] ultrasound strain imaging,[46] and shear wave elastography.[47] Methods providing relative stiffness values, such as ultrasound strain imaging, are not appropriate for use in biomechanical models that employ body forces or prescribe stress components on a boundary. Limitations of other elastography methods include workflow problems (not convenient additions to current IGBS frameworks) and imaging may be performed in positions unrealistic to surgery. Furthermore, the use of dynamic tissue excitation or large compressive forces may result in higher calculated stiffness values as breast tissue stiffness has been shown to be frequency dependent.[48] For these reasons, we designed this supine, gravity-based elastography approach to be most appropriate for use in IGBS systems.

The use of an image guidance system during breast surgery will increase the amount of total patient treatment time. Prior to surgery, patients will undergo a supine MRI exam. For the system proposed here, a total of three supine MRI acquisitions of the breast will be obtained: precontrast, postcontrast enhanced, and gravity excited. Each of these acquisitions involves a 3-min scan. Therefore, the estimated MRI exam time, including patient setup, is 30 min. The calculation of breast stiffness is done after the MRI exam but prior to surgery. Therefore, this calculation adds no direct time to the patient's treatment. Finally, using an image guidance system in the operating room may add additional time to the surgical procedure. This length of time varies among systems depending on registration and computational requirements. In a study of IGS systems used for neurosurgery, the use of IGS systems decreased the time needed for surgery by providing surgeons with superior orientation to anatomical structures.[49] The authors are not aware of a study conducted

in the context of breast surgery that measures the impact of surgery duration when using an image guidance system.

5 Conclusion

In this study, a method to obtain patient-specific homogeneous and heterogeneous breast tissue mechanical properties was tested. In the homogeneous tissue reconstruction setting, which was developed for use in IGBS applications, optimization convergence errors were found to introduce less than a 1-mm error into the guidance system. We demonstrated that the gravity-based stiffness estimation method is also capable of reconstructing heterogeneous stiffness properties with several avenues for future investigations.

Disclosures

The authors have no potential conflicts to disclose.

Acknowledgments

The authors would like to acknowledge the support of the National Institutes of Health through Grant Nos. K25CA204599 and R21EB022380 and the National Science Foundation for a Graduate Research Fellowship awarded to R.H.G.

References

1. A. M. Schulman et al., "Reexcision surgery for breast cancer: an analysis of the American Society of Breast Surgeons (ASBrS) MasterySM database following the SSO-ASTRO 'No Ink on Tumor' guidelines," *Ann. Surg. Oncol.* **24**(1), 52–58 (2017).
2. R. Jeevan et al., "Reoperation rates after breast conserving surgery for breast cancer among women in England: retrospective study of hospital episode statistics," *BMJ* **345**, e4505 (2012).
3. K. Spilsbury et al., "Subsequent surgery after initial breast conserving surgery: a population based study," *ANZ J. Surg.* **75**(5), 260–264 (2005).
4. L. G. Wilke et al., "Repeat surgery after breast conservation for the treatment of stage 0 to II breast carcinoma: a report from the National Cancer Data Base, 2004–2010," *JAMA Surg.* **149**(12), 1296–1305 (2014).
5. J. Landercasper et al., "Reasons for re-excision after lumpectomy for breast cancer: insight from the American Society of Breast Surgeons MasterySM database," *Ann. Surg. Oncol.* **21**(10), 3185–3191 (2014).
6. L. Langhans et al., "Reoperation rates in ductal carcinoma in situ vs invasive breast cancer after wire-guided breast-conserving surgery," *JAMA Surg.* **152**(4), 378–384 (2017).
7. K. A. Skinner et al., "Palpable breast cancers are inherently different from nonpalpable breast cancers," *Ann. Surg. Oncol.* **8**(9), 705–710 (2001).
8. N. M. A. Krekel et al., "Intraoperative ultrasound guidance for palpable breast cancer excision (COBALT trial): a multicentre, randomised controlled trial," *Lancet Oncol.* **14**(1), 48–54 (2013).
9. C. H. Lee et al., "Breast cancer screening with imaging: recommendations from the Society of Breast Imaging and the ACR on the use of mammography, breast MRI, breast ultrasound, and other technologies for the detection of clinically occult breast cancer," *J. Am. Coll. Radiol.* **7**(1), 18–27 (2010).
10. C. K. Kuhl et al., "Mammography, breast ultrasound, and magnetic resonance imaging for surveillance of women at high familial risk for breast cancer," *J. Clin. Oncol.* **23**(33), 8469–8476 (2005).
11. M. S. Group, "Screening with magnetic resonance imaging and mammography of a UK population at high familial risk of breast cancer: a prospective multicentre cohort study (MARIBS)," *Lancet* **365**(9473), 1769–1778 (2005).
12. L. Turnbull et al., "Comparative effectiveness of MRI in breast cancer (COMICE) trial: a randomised controlled trial," *Lancet* **375**(9714), 563–571 (2010).
13. C. Kuhl et al., "Pre-operative staging of breast cancer with breast MRI: one step forward, two steps back?" *Breast* **16**, 34–44 (2007).
14. N. Houssami et al., "Accuracy and surgical impact of magnetic resonance imaging in breast cancer staging: systematic review and meta-analysis in detection of multifocal and multicentric cancer," *J. Clin. Oncol.* **26**(19), 3248–3258 (2008).
15. V. Gonzalez et al., "Preoperative MRI of the breast (POMB) influences primary treatment in breast cancer: a prospective, randomized, multicenter study," *World J. Surg.* **38**(7), 1685–1693 (2014).
16. J. S. Sung et al., "Preoperative breast MRI for early-stage breast cancer: effect on surgical and long-term outcomes," *Am. J. Roentgenol.* **202**(6), 1376–1382 (2014).
17. L. Esserman et al., "Utility of magnetic resonance imaging in the management of breast cancer: evidence for improved preoperative staging," *J. Clin. Oncol.* **17**(1), 110 (1999).
18. U. Fischer et al., "The influence of preoperative MRI of the breasts on recurrence rate in patients with breast cancer," *Eur. Radiol.* **14**(10), 1725–1731 (2004).
19. C. K. Kuhl et al., "MRI for diagnosis of pure ductal carcinoma in situ: a prospective observational study," *Lancet* **370**(9586), 485–492 (2007).
20. M. D. Pickles et al., "Comparison of 3.0 T magnetic resonance imaging and x-ray mammography in the measurement of ductal carcinoma in situ: a comparison with histopathology," *Eur. J. Radiol.* **84**(4), 603–610 (2015).
21. J. A. Pain et al., "Assessment of breast cancer size: a comparison of methods," *Eur. J. Surg. Oncol.* **18**(1), 44–48 (1992).
22. M. J. Pallone et al., "Supine breast MRI and 3D optical scanning: a novel approach to improve tumor localization for breast conserving surgery," *Ann. Surg. Oncol.* **21**(7), 2203–2208 (2014).
23. H. Satake et al., "Prediction of prone-to-supine tumor displacement in the breast using patient position change: investigation with prone MRI and supine CT," *Breast Cancer* **23**(1), 149–158 (2016).
24. P. Siegler et al., "Supine breast MRI," *J. Magn. Reson. Imaging* **34**(5), 1212–1217 (2011).
25. T. H. Kim, D. K. Kang, and Y. S. Jung, "MR-navigated ultrasound with supine breast MRI for suspicious enhancing lesions not identified on second-look ultrasound in breast cancer patients," *Ultraschall Med.* **37**(S01), SL16_3 (2016).
26. D. K. Kang et al., "Clinical utility of real-time MR-navigated ultrasound with supine breast MRI for suspicious enhancing lesions not identified on second-look ultrasound," *Ultrasound Med. Biol.* **43**(2), 412–420 (2017).
27. M. A. Mallory et al., "Feasibility of intraoperative breast MRI and the role of prone versus supine positioning in surgical planning for breast-conserving surgery," *Breast J.* **23**(6), 713–717 (2017).
28. R. H. Conley et al., "Realization of a biomechanical model-assisted image guidance system for breast cancer surgery using supine MRI," *Int. J. Comput. Assist. Radiol. Surg.* **10**(12), 1985–1996 (2015).
29. R. H. Conley et al., "Image to physical space registration of supine breast MRI for image guided breast surgery," *Proc. SPIE* **9036**, 90362N (2014).
30. T. Alderliesten et al., "On the feasibility of MRI-guided navigation to demarcate breast cancer for breast-conserving surgery," *Med. Phys.* **37**(6), 2617–2626 (2010).
31. L. W. Clements et al., "Evaluation of model-based deformation correction in image-guided liver surgery via tracked intraoperative ultrasound," *J. Med. Imaging* **3**(1), 015003 (2016).
32. H. O. Altamar et al., "Kidney deformation and intraprocedural registration: a study of elements of image-guided kidney surgery," *J. Endourol.* **25**(3), 511–517 (2011).
33. K. K. Brock et al., "Feasibility of a novel deformable image registration technique to facilitate classification, targeting, and monitoring of tumor and normal tissue," *Int. J. Radiat. Oncol. Biol. Phys.* **64**(4), 1245–1254 (2006).
34. M. I. Miga, "Computational modeling for enhancing soft tissue image guided surgery: an application in neurosurgery," *Ann. Biomed. Eng.* **44**(1), 128–138 (2016).
35. R. H. Griesenauer et al., "Breast tissue stiffness estimation for surgical guidance using gravity-induced excitation," *Phys. Med. Biol.* **62**(12), 4756–4776 (2017).
36. J. Georgii and R. Westermann, "Corotated finite elements made fast and stable," in *Workshop in Virtual Reality Interactions and Physical Simulation "VRIPHYS"*, Vol. 8, pp. 11–19 (2008).

37. J. A. Weis et al., "Assessing the accuracy and reproducibility of modality independent elastography in a murine model of breast cancer," *J. Med. Imaging* **2**(3), 036001 (2015).
38. J. J. Ou et al., "Evaluation of 3D modality-independent elastography for breast imaging: a simulation study," *Phys. Med. Biol.* **53**(1), 147–163 (2008).
39. E. Polak and G. Ribiere, "Note sur la convergence de méthodes de directions conjuguées," *ESAIM Math. Modell. Numer. Anal.* **3**(R1), 35–43 (1969).
40. R. Fletcher and C. M. Reeves, "Function minimization by conjugate gradients," *Comput. J.* **7**(2), 149–154 (1964).
41. K. Levenberg, "A method for the solution of certain non-linear problems in least squares," *Q. Appl. Math.* **2**(2), 164–168 (1944).
42. D. W. Marquardt, "An algorithm for least-squares estimation of nonlinear parameters," *J. Soc. Ind. Appl. Math.* **11**(2), 431–441 (1963).
43. R. G. Abramson et al., "Age-related structural and functional changes in the breast: multimodality correlation with digital mammography, computed tomography, magnetic resonance imaging, and positron emission tomography," *Semin. Nucl. Med.* **37**(3), 146–153 (2007).
44. N. N. Y. Janssen et al., "Supine breast MRI using respiratory triggering," *Acad. Radiol.* **24**, 818–825 (2017).
45. Y. K. Mariappan, K. J. Glaser, and R. L. Ehman, "Magnetic resonance elastography: a review," *Clin. Anat.* **23**(5), 497–511 (2010).
46. I. Cespedes et al., "Elastography: elasticity imaging using ultrasound with application to muscle and breast in vivo," *Ultrason. Imaging* **15**(2), 73–88 (1993).
47. W. Meng et al., "Preliminary results of acoustic radiation force impulse (ARFI) ultrasound imaging of breast lesions," *Ultrasound Med. Biol.* **37**(9), 1436–1443 (2011).
48. N. G. Ramião et al., "Biomechanical properties of breast tissue, a state-of-the-art review," *Biomech. Model. Mechanobiol.* **15**, 1307–1323 (2016).
49. M. Luz, G. Strauss, and D. Manzey, "Impact of image-guided surgery on surgeons' performance: a literature review," *Int. J. Hum. Factors Ergon.* **4**(3–4), 229–263 (2016).

Biographies for the authors are not available.